Icarus 387 (2022) 115223

Contents lists available at ScienceDirect

Icarus

journal homepage: www.elsevier.com/locate/icarus

Pre and post-landing atmospheric optical depths at the Zhurong landing site on Mars retrieved using a single-image-based approach

Wai Chung Liu [a], Bo Wu [a,*], Zhaojin Li [a], Jie Dong [b], Wei Rao [b]

[a] Planetary Remote Sensing Laboratory, Department of Land Surveying & Geo-Informatics, The Hong Kong Polytechnic University, Hung Hom, Kowloon, Hong Kong, PR China

[b] China Academy of Space Technology, 104 Youyi Street, Haidian, Beijing, PR China

ARTICLE INFO

Keywords:
Mars
Atmospheric optical depth
Monocular images
DISORT
Zhurong landing site

ABSTRACT

The atmosphere of Mars has complex photometric processes due to multiple scattering and absorption by the suspended aerosols. The atmospheric optical depth is an indicator of the aerosol concentrations and can be used to model the contribution of atmospheric scattering, thereby correcting surface spectra. The atmospheric optical depth is also important in analysing the variations of atmospheric dust and evaluating the risks facing landing and roving missions. Retrieving the atmospheric optical depth from a single image is desirable as simultaneous stereo observations of the Martian surface are not common. However, most of the existing single-image-based methods rely on shadows in the image, which can be challenging to identify when the site is smooth or when the atmosphere becomes turbid. In this paper, we present a method of retrieving the atmospheric optical depth from a single image based solely on non-shadowed surfaces. This method was validated using HiRISE images and measurements acquired by rovers on the Martian surface. The method achieved an RMSE of 2%–7% in most cases, depending on the different surface photometric models used. The results indicated that aerosol scattering parameters have less impact on the retrievals than the surface photometric properties, likely due to the fact that the data is optically thin. The optical depths at the Zhurong landing site before and after landing were estimated using the proposed method. The results show that the optical depths first decreased and then increased, with the turning point being around the landing date, indicating that the Zhurong rover landed at an appropriate time. The proposed method is of significance for the analysis of Martian atmospheric dust and surface spectra with better spatio-temporal resolutions.

1. Introduction

Mars is engulfed by a thin atmosphere that gives rise to its climatic variations and prevailing aeolian processes. Aerosols (e.g., dust and ice) suspended in the atmosphere scatter the incoming solar radiation and thus affect the amount of energy received by the surface. This process affects the planet's photometry and energy budget and may pose risks to lander and rover operations (e.g., a decrease in solar energy production and a loss of contact) (Gebhardt and Abuelgasim, 2019). The aerosol concentration can be characterised by the optical depth, which describes the transmissivity of light within an atmosphere. Therefore, the optical depth is often of interest in clarifying the spatio-temporal distributions of Martian aerosols and their implications for the planet's weather and climate (Montabone et al., 2015), photometric characteristics, and hazard assessments.

Optical depth measurements have been widely used in Martian climatology. This includes studies such as inferring the microphysical structure of aerosols (e.g., Lemmon et al., 2004; Wolff et al., 2009), temporal variations of the Martian atmosphere (e.g., Colburn et al., 1989; Montabone et al., 2015; Tang et al., 2021; Wolkenberg and Giuranna, 2021), and characterisation of dust storms and dust devils (e.g., Reiss et al., 2014; Viúdez-Moreiras et al., 2019). Optical depth measurements have also been used for cartographic purposes such as photometric normalization (e.g., Kirk et al., 2000). In addition, the optical depth is critical for photoclinometric 3D reconstruction of the Martian surface (e.g., Wu et al., 2018; Hess et al., 2019; Doute and Jiang, 2020; Liu and Wu, 2020; Chen et al., 2021) because of the light scattering by the atmosphere.

* Corresponding author at: Planetary Remote Sensing Laboratory, Department of Land Surveying and Geo-Informatics, The Hong Kong Polytechnic University, Hung Hom, Kowloon, Hong Kong.
E-mail address: bo.wu@polyu.edu.hk (B. Wu).

https://doi.org/10.1016/j.icarus.2022.115223
Received 20 December 2021; Received in revised form 4 July 2022; Accepted 10 August 2022
Available online 17 August 2022

The atmospheric optical depth can be estimated using various methods. For example, limb-geometry observations, acquired by orbiter payloads such as the Thermal Emission Spectrometer (TES) of the Mars Global Surveyor, the Planetary Fourier Spectrometer and Observatoire pour la Minéralogie, l'Eau, les Glaces et l'Activité (OMEGA) of Mars Express. Measurements from the Mars Climate Sounder of the Mars Reconnaissance Orbiter (MRO) are ideal for understanding the vertical structure of the Martian atmosphere (Smith, 2008; D'Aversa et al., 2021). However, these data are usually of lower spatial resolution and are thus more suitable for global analysis. Nadir pointing thermal data (e.g., TES nadir observations) were widely used for dust and water-ice aerosol optical depth retrieval since the scattering component of these two types of aerosols can be neglected in the thermal spectrum (Smith, 2004). Multi-view observations such as those obtained by the Compact Reconnaissance Imaging Spectrometer for Mars (CRISM) of MRO and OMEGA of Mars Express provide simultaneous acquisitions of the exact surface location at multiple viewing angles, allowing the analysis of the emission phase function (Doute and Ceamanos, 2010; Vincendon, 2013). Because light scattered to each emission angle travels along different optical paths through the atmosphere, a more reliable estimation of the atmospheric optical depth can be obtained (Ceamanos et al., 2013). Since CRISM and OMEGA data are often used to analyse the surface spectral characteristics (Ceamanos et al., 2013; Vincendon, 2013), the optical depth and Radiative Transfer Models (RTMs) of the atmosphere have to be determined for the optimal retrieval of surface spectra. There are several ways to construct an RTM for the atmosphere, such as the discrete ordinate method (McGuire et al., 2008; Doute and Ceamanos, 2010) and Monte-Carlo simulations (Vincendon et al., 2007; Vincendon, 2013). Different methods require knowledge of the scattering characteristics of the aerosols, which have been studied using rover observations (Ockert-Bell et al., 1997; Tomasko et al., 1999) and satellite observations (e.g., Wolff et al., 2009, 2010).

Mars landers and rovers provide in-situ observations for retrieving optical depths. The Sun-viewing images obtained by the landers or rovers were used to measure the direct extinction of sunlight (Lemmon et al., 2004). Optical depths measured by sensors on-board the Viking landers and Mars Exploration Rovers (MERs) (i.e., Spirit and Opportunity rovers) were used for understanding the characteristics and evolution of the Martian atmosphere (Colburn et al., 1989; Lemmon et al., 2004, 2015). Optical depth observations provided by the Mars Science Laboratory (MSL) (i.e., Curiosity rover) (Lemmon, 2014; Chen-Chen et al., 2019) have been studied for various applications such as the impact of dust storms (Viúdez-Moreiras et al., 2019). In addition, ground-based observations provide essential constraints on the forward scattering characteristics of the aerosols (Chen-Chen et al., 2019). Optical depths measured from the surface are usually accurate and often treated as references for validating retrievals based on orbital data (Hoekzema et al., 2011; Petrova et al., 2012; Tang et al., 2021). However, such measurements are highly limited by the locations and operation times of the landers and rovers.

Among methods of retrieving the optical depth, methods based on optical images such as images of the High Resolution Stereo Camera (HRSC) (Neukum et al., 2009) and High Resolution Imaging Science Experiment (HiRISE) (McEwen et al., 2007) are of interest for applications such as photoclinometry. The stereo method proposed by Hoekzema et al. (2010) exploits the difference in the optical path between the nadir and off-nadir HRSC images acquired simultaneously. Li et al. (2021) adopted this method to obtain an initial estimate of the optical depth for photoclinometric reconstruction based on simultaneously acquired stereo HRSC images. However, the method is not suitable for applications when only a single image is available. Hoekzema et al. (2011) proposed a single-image optical depth retrieval method, known as the shadow method, which relies on the intensity difference between illuminated and shadowed pixels. Although this method does not require additional data, the resulting optical depths deviated from actual depths because of the simplifications and assumptions made. Therefore, the retrieved optical depth must be corrected empirically using in-situ observations made by rovers (Hoekzema et al., 2011). Tang et al. (2021) applied this method to characterise the temporal variations in the optical depth near the Tianwen-1 (Zhurong rover) landing site (Wu et al., 2021; Wu et al., 2022) before the landing. A more sophisticated shadow method (Petrova et al., 2012) incorporates a digital elevation model (DEM) and an RTM to model the atmosphere. The method uses a numerical scheme to simultaneously obtain the surface albedo and optical depth from imagery samples. Hess et al. (2019) used a similar but simplified method in their photoclinometric reconstruction approach. They used a DEM and a simplified Top-of-Atmosphere (TOA) model to estimate an image's most probable optical depth. To ensure plausible results, their method requires fitting over a large number of sample points and useful shadows.

The aforementioned single-image-based methods require shadows for parameter retrieval. However, true shadows are not always common on the Martian surface. Additionally, it can be challenging to accurately detect shadows when the sky becomes turbid because one may not be able to distinguish a shadowed surface from an illuminated surface facing away from the Sun, or dark albedo patches. Moreover, the radiance observed in areas of shadows is affected by various factors, such as the size of and distance from the shadow caster, the spatial resolution of the image, and circumsolar aureole (Thomas et al., 1999). These factors introduce additional uncertainty to the determination of shadow photometry, and hence optical depth retrieval.

In contrast, illuminated surfaces of different orientations can easily be found on Mars. Therefore, in this paper, we present a novel approach of retrieving the optical depth from a single image that does not require shadows or observations made by other sensors. The proposed method models the TOA photometry of an image using a co-registered DEM, and then characterises the optical depth using an RTM of the Martian atmosphere. The DEM can be obtained through photogrammetry or laser altimetry or from historical data (e.g., Kirk et al., 2008; Li et al., 2021). The RTM can be built using radiative transfer solutions (e.g., Stamnes et al., 1988) and the photometric properties of the Martian aerosols (e.g., Ockert-Bell et al., 1997). The approach does not require observations acquired by other sensors (e.g., OMEGA and CRISM), and it is thus not limited by the extra data availability or spatial resolution of additional data. Moreover, the method is convenient to apply as it uses only illuminated surfaces. We expect the proposed method will enable more automated measurement of optical depths on Mars from the vast amount of available high-resolution image datasets, which will contribute to the more localised and detailed characterisation of the Martian atmosphere and facilitate Mars climate studies and other research topics related to the atmosphere.

This paper is organised as follows. Section 2 describes the rationale and the details of the proposed approach, and validates the proposed approach using HiRISE images and optical depth measurements obtained from MERs and the MSL rover. Section 3 applies the proposed approach in deriving and analysing the temporal trend of the atmospheric optical depths at the Tianwen-1 (Zhurong rover) landing site before and after landing. In Section 4, we summarise the findings and provide concluding remarks.

2. Single-image-based atmospheric optical depth retrieval approach

2.1. Overview of the approach

The rationale of the approach is as follows. It uses two ways to compute the same atmospheric scattering quantity which is related to the optical depth. The first way relies solely on an RTM and no information about the surface is required. The second way derives the same quantity from the image and the corresponding topography. The approach then estimates the most likely optical depth such that the resulted quantities from the two ways converge.

The overall workflow of the approach is illustrated in Fig. 1. It is assumed that an image is orthorectified and co-registered with a DEM. The imaging conditions (i.e., the illumination and viewing geometries) must be known. We first extract multiple samples from the image and their corresponding topography from the DEM. The surface reflectance of each sample is then computed using a surface photometric model and the known imaging conditions. We calculate two types of surface reflectance per sample: the bidirectional reflectance, which describes surface reflectance from direct illumination, and the hemispherical-directional reflectance, which describes surface reflectance from diffuse illumination (i.e., skylight). Using the computed surface reflectance of each sample and the corresponding image intensity, a linear model is fitted for the set of samples. The aerosol scattering component is then estimated for a predefined optical depth. Additionally, an atmospheric scattering model can be built using an RTM, such as DISORT (Stamnes et al., 1988), with known imaging conditions and photometric properties of the Martian atmosphere. The atmospheric scattering model describes the levels of diffuse illumination and aerosol scattering for various optical depths. The model therefore offers an independent way of obtaining the aerosol scattering component for any predefined optical depth. Furthermore, the diffuse illumination component derived from the RTM is used to increase the robustness and reliability of the DEM estimation routine.

The optical depth can then be derived by minimising the difference between the aerosol scattering component estimated from the DEM data and that simulated using the RTM. The aerosol scattering component is selected for the optimisation criterion because it is independent of surface scattering. The aerosol scattering component can thus be effectively simulated using the RTM and estimated from DEM samples without prior knowledge of the surface albedo. Additionally, the strategy has a computational advantage over methods that require the surface albedo and optical depth to be numerically simulated (e.g., Petrova et al., 2012).

2.2. Estimation of atmospheric aerosol scattering from a single image using a DEM

2.2.1. TOA photometric model of the Martian surface

The TOA photometric model describes the radiance observed by the sensor after scattering and absorption by the atmosphere and the surface. Orbiter images are often considered TOA observations because they are acquired far above the topmost layer of the planetary atmosphere. With the presence of the atmosphere, the scattering of the surface becomes complex. In general, the overall process can be broken down into several components (Petrova et al., 2012), encompassing direct and indirect illumination and scattering at the surface, multiple scattering in the atmosphere, and photometric interactions occurring solely with aerosols. For practical reasons, not all of the components are included to formulate the TOA model: e.g., Gehrke (2008) only considered bidirectional reflectance of the surface and aerosol scattering, whereas Hess et al. (2019) also included diffuse illumination of the surface. We followed the convention of Hess et al. (2019) and formulated the TOA model as follows:

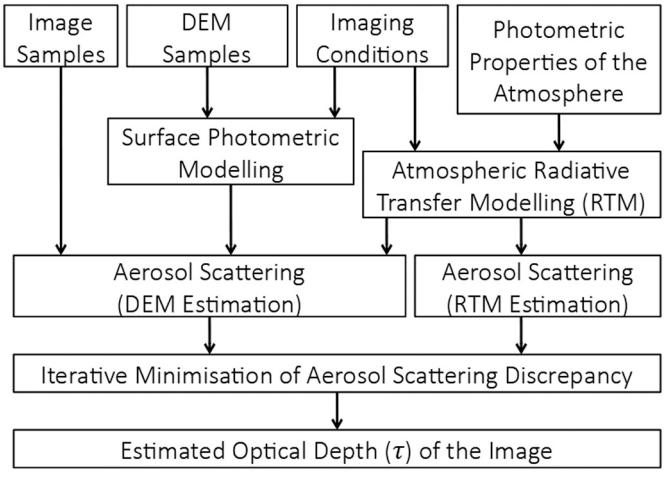

Fig. 1. Overall workflow of the optical depth retrieval approach. It computes the same atmospheric quantity (i.e., aerosol scattering) using two methods. The most likely optical depth is obtained by converging the two computed aerosol scattering.

$$I_{TOA} = \omega e^{-\tau\left(\frac{1}{\mu_{0F}}+\frac{1}{\mu_F}\right)} R_{dd} + \omega\beta(\tau)e^{-\tau\frac{1}{\mu_F}}R_{hd} + \alpha(\tau), \quad (1)$$

where I_{TOA} is the TOA radiance factor (I/F) observed by the sensor and normalised by a perfectly reflecting lambert surface (Hapke, 2012). ω is the surface albedo, and τ is the atmospheric optical depth. μ_{0F} and μ_F are respectively the incidence and emission angle cosines relative to a flat surface. R_{dd} and R_{hd} are the bidirectional and hemispherical-directional reflectances of the surface, respectively. $e^{-\tau\frac{1}{\mu_{0F}}}$ and $e^{-\tau\frac{1}{\mu_F}}$ are the atmospheric attenuation factors of the incident and reflected light according to the Beer-Lambert law. Because R_{dd} is affected by the atmospheric attenuation of both incoming and outgoing light, and its attenuation factor is thus $e^{-\tau\frac{1}{\mu_{0F}}} \times e^{-\tau\frac{1}{\mu_F}} = e^{-\tau\left(\frac{1}{\mu_{0F}}+\frac{1}{\mu_F}\right)}$. R_{hd} is the reflection of the surface under diffuse illumination, hence it is only affected by the attenuation of outgoing light. $\beta(\tau)$ is the diffuse illumination received by the surface. $\alpha(\tau)$ is the irradiation that is scattered by aerosols and never interacts with the surface. For simplification, we made two assumptions for $\beta(\tau)$: First, we ignore that the Martian skylight is not uniform (Davis and Soderblom, 1984; Thomas et al., 1999) and assume $\beta(\tau)$ is independent of the surface orientation. Second, we ignore the light scattered from the surface that is re-scattered diffusely back onto the surface, hence $\beta(\tau)$ is independent of surface albedo. Furthermore, $\alpha(\tau)$ and $\beta(\tau)$ can be constructed using RTMs (Petrova et al., 2012) or Monte-Carlo simulations (Vincendon et al., 2007). In either case, the photometric properties of the atmosphere must be known.

2.2.2. Estimation of the aerosol scattering parameter

Several samples need to be collected from the image and their corresponding topography obtained from the DEM for the estimation of the aerosol scattering parameter. The sample set has the following characteristics. (1) The sample set has a relatively homogenous surface albedo such that ω can be assumed constant. (2) The sample set consists of multiple surface orientations such that R_{dd} and R_{hd} are different for each sample. (3) The sample set is not shadowed, such that R_{dd} is valid for each sample. Typical examples of such samples include the inner part of a crater, a peak, or a cone. The goal is to use Eq. (1) to search for the aerosol scattering parameter α that best fits the sample set, for a given τ. The parameter α depends on τ and is additive in nature and independent of surface scattering (i.e., independent of ω, R_{dd} and R_{hd}). The parameter α can therefore be effectively delineated from the rest of Eq. (1) and can be used to estimate the optical depth τ. To this end, Eq. (1) is further factorised as:

$$I_{TOA}(\tau) = \omega\left[e^{-\tau\left(\frac{1}{\mu_{0F}}+\frac{1}{\mu_F}\right)} R_{dd} + \beta(\tau)e^{-\tau\frac{1}{\mu_F}}R_{hd}\right] + \alpha_{DEM}. \quad (2)$$

The equation shows that the relative contribution of R_{dd} and R_{hd} depends only on τ and $\beta(\tau)$, which can be modelled using the RTM without prior knowledge of ω under our assumptions. Note that such factorisation is only possible for surface photometric models linearly dependent on the albedo; several typical models are discussed in the next section. More complex considerations are needed for models that depend non-linearly on the albedo, such as the Hapke model (Hapke, 2012). Then, using a photometric model to compute R_{dd} and R_{hd} from

the DEM, Eq. (2) is applied to each of the samples and an equation set is constructed. As a result, for any given τ, only ω and α_{DEM} remain unknown, and they can be estimated by taking the least-squares approach:

$$argmin_{\omega,\alpha_{DEM}} \sum_{k\in K} \left[I_{TOA}(\tau_n)_k - I_k \right]^2, \tag{3}$$

where τ_n is a given τ. The fitting is linear, and ω and α_{DEM} are essentially the slope and the y-intercept of the fitted line. The surface albedo ω is not used by the approach. We deliberately avoid using an RTM to model α_{DEM} and leave α_{DEM} to be fitted by a linear least-squares approach. This is because α_{DEM} will be used as an observation constraint in searching for the best τ, as further explained in the following section. However, to ensure optimisation stability, an RTM is still used to constrain α_{DEM} by providing an estimated $\beta(\tau)$.

2.2.3. Surface photometric models

The bidirectional reflectance of the surface R_{dd} can be described using various photometric models (e.g., Fairbairn, 2005; Shkuratov et al., 2011; Hapke, 2012). In this study, we test several models commonly used in Martian photometry (Soderblom et al., 2006), namely the Lambert model, the Lunar-Lambert model (LL model) (McEwen, 1991, 1996) and the Minnaert model (Minnaert, 1941). The Lambert model is defined by the incidence angle cosine between the vector pointing to the Sun and the normal vector of the surface:

$$R_{dd}(\mu_0) = \mu_0. \tag{4}$$

The Minnaert model is defined as (Soderblom et al., 2006):

$$R_{dd}(\mu_0, \mu, g) = \pi p(g) \mu_0^{k(g)} \mu^{1-k(g)}, \tag{5}$$

where μ_0 and μ are respectively the incidence and emission angle cosines relative to the surface normal. $k(g)$ depends on the phase angle g and determines the relationship between μ_0 and μ of the model, and $p(g)$ is a single-scattering phase function that describes the scattering preference of the Martian regolith. For Mars, we adopted the parameters for $k(g)$ and $p(g)$ from USGS's Integrated Software for Imagers and Spectrometers (ISIS) documentation (https://isis.astrogeology.usgs.gov/Application/presentation/Tabbed/photemplate/photemplate.html).

The LL model is a linear combination of the Lambert model and the Lommel-Seeliger model and is formulated as

$$R_{dd}(\mu_0, \mu, g) = \left[(1 - \lambda(g))\mu_0 + 2\lambda(g) \frac{\mu_0}{\mu_0 + \mu} \right] p(g), \tag{6}$$

where the phase-dependent function $\lambda(g)$ controls the relative contribution of the two major components within the model. We also adopted the parameters for $\lambda(g)$ and $p(g)$ from the ISIS documentation. The above models have far fewer parameters than other more sophisticated models (e.g., the Hapke model). This is desirable for single-image applications where the observations are limited. Furthermore, the models are linearly dependent on surface albedo ω, which can be factorised to simplify the optical depth retrieval.

The hemispherical-directional reflectance R_{hd} describes the scattering by a surface that is diffusely illuminated by the atmosphere. R_{hd} can be modelled by integrating R_{dd} over all possible illumination directions in the upper hemisphere of the surface for the same outgoing direction.

$$R_{hd}(\mu) = \int_{\phi=0}^{2\pi} \int_{\mu_0=0}^{1} R_{dd}, \tag{7}$$

where ϕ is the illumination azimuth in radians. The integration over the upper hemisphere covers all illumination azimuths ($0 \le \phi \le 2\pi$) and incidence angles between 0° and 90°, translating to ($0 \le \mu_0 \le 1$). Because the phase-dependent functions adopted from the ISIS documentation ($k(g)$, $\lambda(g)$ and $p(g)$) are expressed as tabulated lists of function outputs with respect to a list of specified phase angles (0°-180° with 10° interval), analytical forms of these functions are not straightforward. Therefore, to avoid the potentially complicated analytical formulations resulting from the phase-dependent components, we approximated a set of $R_{hd}(\mu)$ numerically by using the trapezoidal rule for a set of predefined μ within the range $0 \le \mu \le 1$. $R_{hd}(\mu)$ for any specific μ is then interpolated from the set.

2.3. Derivation of Martian atmospheric quantities using a radiative transfer model

2.3.1. Discrete ordinate method for atmospheric light scattering

We used the discrete ordinate method to model the radiative transfer processes of the Martian atmosphere. The approach solves radiative transfer equations of a plane-parallel medium by discretising all propagation directions into multiple streams (Stamnes et al., 1988; Hapke, 2012) and computes the intensity of light travelling along any designated path, accounting for radiative processes such as multiple scattering and absorption by the aerosols. The approach is widely adopted to solve the radiative transfer equations (Hapke, 2012) and has been adopted in studying the photometry of planetary surfaces and atmospheres (e.g., McGuire et al., 2008; Doute and Ceamanos, 2010; Ceamanos et al., 2013).

We customised the discrete ordinate method package implemented by Stamnes et al. (1988), known as DISORT (version 4, http://www.rtatmocn.com/disort/), to our use case on Mars. The main quantities required for our approach are $\beta(\tau)$, the amount of diffuse illumination from the sky, and $\alpha(\tau)$, the aerosol path scattering component that does not interact with the surface. The two quantities can be directly computed using DISORT from the illumination and imaging geometry and the photometric properties of the atmosphere (e.g., the single-scattering albedo and phase characteristics). To construct the atmospheric model using DISORT, we consider a single layer of the atmosphere characterised by the average photometric properties of the contained aerosols and a given total optical depth τ. Using a single-layered atmosphere has been demonstrated in previous works (e.g., Vincendon et al., 2007). The photometric properties can be adopted from previous studies on the Martian atmosphere (e.g., Pollack et al., 1995; Ockert-Bell et al., 1997). The quantities $\alpha(\tau)$ and $\beta(\tau)$ are not affected by the surface photometry and can thus be obtained by configuring a perfectly absorbing surface (i.e., $\omega = 0$) at the lower boundary of the atmosphere. As a result, the construction of the atmospheric model does not require prior knowledge of the surface. We then configure the directions of the incident and emerging beams according to the illumination and imaging geometry of the image to be analysed. To ensure flexible and convenient applications, we do not consider more sophisticated properties, such as multiple atmospheric layers, air temperature and pressure. However, whenever necessary, DISORT is capable of modelling complicated atmospheres given sufficient information.

2.3.2. Scattering properties of Martian aerosols

The scattering properties of the aerosol particles have to be known for DISORT to simulate Martian atmospheric scattering. Such properties include the single scattering albedo of the aerosols ω_{atm}, the phase-dependent scattering model $p_{atm}(g)$, and the parameters used to characterise $p_{atm}(g)$. ω_{atm} is used to determine the amount of light absorbed by the atmosphere and propagated downward or upward. $p_{atm}(g)$ describes how a single aerosol particle scatters incoming light at different phase angles and can be modelled using the Single Henyey-Greenstein function (Pollack et al., 1995; Ockert-Bell et al., 1997; Tomasko et al., 1999):

$$p_{atm}(g) = \frac{1 - \varepsilon^2}{\left[1 + \varepsilon^2 - 2\varepsilon cos(g)\right]^{3/2}}, \tag{8}$$

where g is the phase angle and $-1 \le \varepsilon \le 1$ is the asymmetry factor

characterising the directional preference of the scattering particle. $\varepsilon > 0$ implies a forward scatterer whereas $\varepsilon < 0$ implies a backward scatterer. The parameters ε and ω_{atm} vary with wavelength and should therefore be chosen according to the target image's radiometric properties. The present study used HiRISE red-band images with a central wavelength of 700 nm (McEwen et al., 2007). Previous analyses have provided scattering parameters at this wavelength as ($\varepsilon = 0.65$; $\omega_{atm} = 0.94$) (Pollack et al., 1995; Ockert-Bell et al., 1997). Another analysis reported slightly more forward scattering parameters ($\varepsilon = 0.68$; $\omega_{atm} = 0.95$) (Tomasko et al., 1999). More recently, Chen-Chen et al. (2019) reported parameters ($\varepsilon = 0.687$; $\omega_{atm} = 0.975$) based on MSL images and the analysis made by Wolff et al. (2009). We tested all three sets of parameters when validating our approach using MER and MSL data. When applying our approach to the Zhurong landing site, on the other hand, we selected ($\varepsilon = 0.65$; $\omega_{atm} = 0.94$) because this set of parameters was estimated from Viking lander images acquired at solar incidence angles of 53°-64°, which is consistent with that of the HiRISE images that we used (having solar incidence angles of approximately 50°-60°). In contrast, the other two sets were estimated respectively from Pathfinder and MSL images acquired at a solar incidence angle of approximately 75°.

2.3.3. Modelled Martian atmospheric quantities based on DISORT

After constructing the atmospheric model using a predefined τ, the quantity $\beta(\tau)$ is characterised by the relative downward flux, per solid angle, computed from DISORT whereas $\alpha(\tau)$ is characterised by the intensity of the emerging beam leaving the TOA (i.e., the upper boundary of the atmosphere) towards the sensor. Fig. 2 gives examples of the curves of $\alpha(\tau)$ and $\beta(\tau)$ versus τ. We measured the coefficient of variations (i.e., standard deviation divided by mean) for $\alpha(\tau)$ and $\beta(\tau)$ and found that different scattering parameters resulted in variations of <5% for $\alpha(\tau)$ and <8% for $\beta(\tau)$. $\alpha(\tau)$ increases monotonically with τ, whereas $\beta(\tau)$ first increases and then decreases with τ. These trends agreed with the analysis results obtained by other studies (e.g., Petrova et al., 2012).

2.4. Optimisation scheme for the retrieval of the atmospheric optical depth

As aforementioned, this approach uses two ways to compute $\alpha(\tau)$. One way models $\alpha(\tau)$ independently using DISORT. The other way estimates $\alpha(\tau)$ from samples collected from the image and the corresponding DEM, with minimal input (i.e., an estimated $\beta(\tau)$) from DISORT as a constraint for stable optimization. The two estimates represent the same quantity and there exists a τ such that the discrepancy between the two estimates is minimal. The optical depth τ that corresponds to the image can thus be obtained by the least-squares approach:

$$argmin_\tau E(\tau) = (\alpha_{DISORT}(\tau) - \alpha_{DEM}(\tau))^2, \quad (9)$$

where $\alpha_{DISORT}(\tau)$ is the aerosol scattering modelled by the RTM, which is DISORT in this case, and $\alpha_{DEM}(\tau)$ is that estimated from DEM samples. In actual practice, because of the complexity of DISORT or any other radiative transfer models, the least-squares optimisation is performed numerically. First, a predefined set of optical depths, $\tau_{n\in N}$, is constructed, where τ_n is the n^{th} predefined optical depth within a total of N elements. The range of τ must contain the actual optical depth of the image, where $0 \le \tau_n \le 2$ is an appropriate range for our experimental datasets but a greater upper limit is preferred for dusty seasons. Second, for each τ_n, we compute $\alpha_{DISORT}(\tau_n)$ and $\beta(\tau_n)$ using DISORT. Then, we compute $\alpha_{DEM}(\tau_n)$ using Eq. (3) and $\beta(\tau_n)$. Afterwards, we compute $E(\tau_n)$ using Eq. (9). After computing $E(\tau_n)$ for each τ_n, we identify τ_{best}, which is the τ_n that obtained the minimal $E(\tau_n)$. The final optical depth τ is obtained by refining τ_{best} in a least-squares solution.

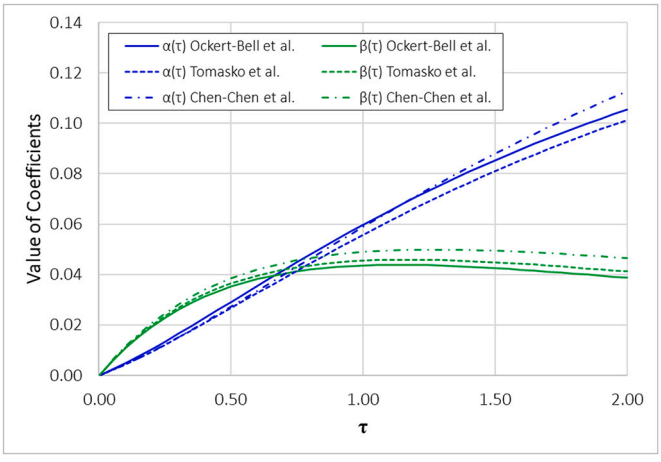

Fig. 2. Curves of $\alpha(\tau)$ and $\beta(\tau)$ versus τ computed by DISORT based on several published aerosol scattering properties assuming a fully absorbing surface (i.e., $\omega = 0$). The imaging conditions are set as an incidence angle of 56.19°, emission angle of 3.84° and phase angle of 59.31°.

2.5. Validation of the approach using MER and MSL observations

To validate the proposed method, we have used the red-band images of the High Resolution Imaging Science Experiment (HiRISE) (McEwen et al., 2007) and the corresponding DEMs constructed through photogrammetry (Kirk et al., 2008) to derive optical depths. In addition, we obtained optical depth observations from the MERs (Opportunity and Spirit) and MSL rover (Curiosity) for reference. The HiRISE images have a spatial resolution of 0.25 m/pixel whereas the photogrammetrically derived DEMs have a spatial resolution of 1 m/pixel. We used HiRISE images acquired at times when the rover was located in the acquisition zone of the sensor. Such images provide observations that are nearly time-synchronous with those of the ground rovers. The accuracy can thus be assessed by comparing the optical depth retrieved using the proposed method with that obtained from rover measurements (Lemmon et al., 2015).

The information of the HiRISE images and their reference optical depths are listed in Table 1. The images were first georeferenced to their corresponding DEMs. The reference optical depths were then obtained from rover observations according to the acquisition date and time, and the relevant rover. For the Opportunity and Spirit rovers, the reference optical depth values were derived from solar filter images of the rover's Panoramic Camera (Pancam) (Lemmon et al., 2004). The optical depth data are available from NASA's Analyst Notebook (https://an.rsl.wustl.edu/). The sol number corresponding to the HiRISE observations is also provided. Both the Opportunity and Spirit rovers have two solar filters, which have a central wavelength of 440 nm (L8 filter) and 880 nm (R8 filter), respectively. However, it is known that the 440 nm filters have suffered red leaks, resulting in the actual central wavelength being approximately 719 nm (Lemmon et al., 2004; Tang et al., 2021). Therefore, the optical depth data from the L8 filter can be used as a reference for analysing HiRISE red band images. To account for the time-of-day variations in optical depth (Colburn et al., 1989), we interpolated the reference values from mid-day and late-afternoon observations of the same sol using the local time of the images. For the Curiosity rover, we used the optical depth reported by Chen-Chen et al. (2019), which was derived from the Sun-viewing images of the rover's Navigation Camera (Navcam) at an effective wavelength of 650 nm (Maki et al., 2012). The reported optical depths did not cover exactly the date of the HiRISE image (sol 597 of Curiosity) and therefore we identified the closest available data points (sols 589 and 631) (Chen-Chen et al., 2019) and interpolated the reference τ using the solar longitude.

We extracted different samples from each of the images and DEMs, as shown in Fig. 3. We selected regions with distinctive topographic variations, such as craters and hills, and sampled Sun-facing and Sun-facing-

Table 1
Information on the HiRISE images used in experimental analysis.

HiRISE Image ID	*PSP_003900_1650_RED*	*TRA_000873_1780_RED*	*ESP_036128_1755_RED*
Acquisition Date	27 May 2007	3 October 2006	11 April 2014
Local Time	15.31	15.45	15.45
Solar Longitude (Ls)	245.87°	115.34°	114.98°
Incidence Angle	47.56°	56.19°	57.45°
Emission Angle	2.60°	3.84°	2.68°
Phase Angle	44.99°	59.31°	59.59°
Rover	Spirit	Opportunity	Curiosity
Reference Optical Depth	0.8319 (Lemmon et al., 2015)	0.4289 (Lemmon et al., 2015)	0.4435 (Chen-Chen et al., 2019)

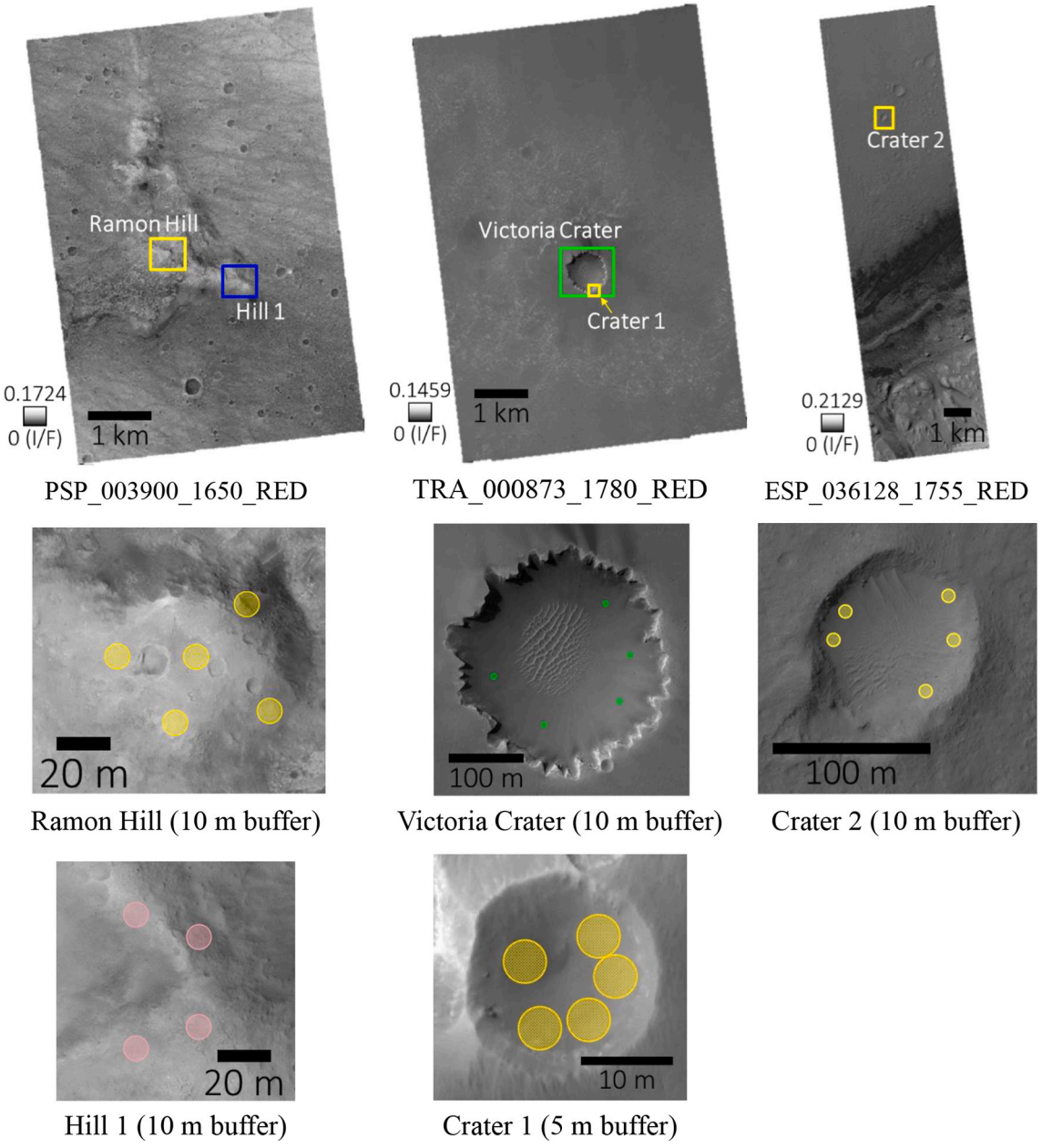

Fig. 3. Samples collected for each experimental dataset.

away slopes of these landforms. Another selection criterion was that we choose landforms with a 'common' albedo, which we believe can be adequately modelled by adopting the default photometric parameters used by ISIS for the Martian surface (Johnson et al., 1999; Kirk et al., 2000). To account for the resolution difference between the images and the DEMs, we created a circular buffer zone centred at each sample point (i.e., circles in Fig. 3) and averaged the required quantities (e.g., light intensity and surface gradients) over the buffer zone for the proposed

method. When determining the buffer radius, we considered such factors as the sizes of landforms and the quality of the DEMs in representing the local topography. We then computed the optical depth τ using the proposed method and tested the three surface photometric models and the three sets of atmospheric scattering parameters. Each sample set has nine possible retrievals based on combinations of surface photometric model and scattering parameters.

The results are summarised in Table 2, with the percentage error of each estimate presented in brackets. We also examined the linear fit between the modelled reflectance (i.e., the square bracketed term in Eq. 2) and those measured on the images in Fig. 4. The linear fits have R^2 values ranging from 0.8 to 0.99, meaning the model adequately describes the data. All samples except for the Hill 1 set achieved <7% Root Mean Square Error (RMSE). Switching atmospheric scattering parameters had less significant effects on retrieval performance, accounting for not more than a few percent. In contrast, switching surface photometric models had a greater impact on the performance, as exemplified by the Hill 1 sample set and the Crater 2 sample set. The greater dependence on surface photometric models is reasonable because the imaged locations are optically thin (i.e., surface features can be clearly seen) and therefore surface photometry has greater effects on the observed radiances. When analysing individual surface photometric models, all of them had a mean error of <7%. The Lambert and Minnaert models had <5% errors in most cases, with the Lambert model slightly outperforming the Minnaert model. A possible reason for the performance of the Lambert model is that the sampled surfaces had smoothed by processes such as erosion and degradation. A consideration of smoothness may also explain why the Lambert model had larger errors for Crater 1 and Crater 2 samples, which had small sand ripples affecting the surface smoothness. In contrast, the parameters used by the LL model and the Minnaert model assume a roughness of 30° (Kirk et al., 2000), which may explain the performances of these models. Another possible reason for the performance of the Lambert model could be that the simplifications made for the TOA model resulted in the overall radiance being better described by the Lambert model. The LL model performed better when the optical depth τ was smaller, which suggests that this model relies more on direct scattering (R_{dd}) than indirect scattering (R_{hd}).

Note that the proposed approach did not consider several skylight-related factors, such as the skyview factor and inhomogeneous skylight, which dictate the amount of skylight received by a surface (Spiga and Forget, 2008; Petrova et al., 2012). The TOA model is also simplified by neglecting a few multiple scattering processes (Hess et al., 2019). Despite these simplifications, the experimental results showed desirable retrieval. One possible reason for desirable retrieval results is the use of non-shadowed samples, where direct illumination and scattering dominate and outweigh the uncertainties introduced by the simplifications made in the indirect scattering domain.

Table 2
Optical depth derived from various samples using the proposed approach. Numbers in brackets are percentage errors relative to the rover observations.

		Lambert Model Ock/Tom/ Chen	LL Model Ock/ Tom/ Chen	Minnaert Model Ock/Tom/ Chen	RMSE
Spirit $\tau = 0.8319$ *for reference*	Ramon Hill	0.809/ 0.815/ 0.787 (2.8/ 2.0/ 5.4%)	0.900/ 0.914/ 0.882 (8.2/ 9.9/ 6.0%)	0.869/ 0.882/ 0.851 (4.5/ 6.0/ 2.3%)	0.048 (5.8%)
	Hill 1	0.868/ 0.876/ 0.845 (4.3/ 5.3/ 1.6%)	0.967/ 0.981/ 0.945 (16.2/ 17.9/ 13.6%)	0.941/ 0.955/ 0.922 (13.1/ 14.8/ 10.8%)	0.101 (12.1%)
Opportunity $\tau = 0.4289$ *for reference*	Victoria Crater	0.426/ 0.432/ 0.421 (0.7/ 0.7/ 1.8%)	0.414/ 0.423/ 0.414 (3.5/ 1.4/ 3.5%)	0.436/ 0.445/ 0.436 (1.7/ 3.8/ 1.7%)	0.010 (2.4%)
	Crater 1	0.450/ 0.456/ 0.444 (4.9/ 6.3/ 3.5%)	0.428/ 0.436/ 0.427 (0.2/ 1.7/ 0.4%)	0.453/ 0.462/ 0.452 (5.6/ 7.7/ 5.4%)	0.020 (4.7%)
Curiosity $\tau = 0.4435$ *for reference*	Crater 2	0.399/ 0.401/ 0.390 (10.0/ 9.6/ 12.1%)	0.462/ 0.469/ 0.456 (4.2/ 5.7/ 2.8%)	0.431/ 0.437/ 0.426 (2.8/ 1.5/ 3.9%)	0.030 (6.8%)
Mean Deviation		4.7%	6.3%	5.7%	

Note: "Ock" stands for the used scattering parameters reported by Ockert-Bell et al. (1997); "Tom" stands for those from Tomasko et al. (1999); and "Chen" stands for those from Chen-Chen et al. (2019).

3. Pre and post-landing atmospheric optical depths at the Zhurong landing site

The Chinese Mars rover Zhurong, onboard the Tianwen-1 probe, successfully landed on Mars on 15 May 2021 (Wu et al., 2022). HiRISE had imaged the Zhurong landing site and its surrounding regions before and after the landing. The landing site was relatively smooth, and most shadows were thus created by boulders and rocks around the flanks of craters. The shadows were therefore small in size and mainly located on slopes. In contrast, there are plenty of landforms that can be used by the proposed method. We applied our method to analyse the optical depth of the Zhurong landing site before and after the landing using the HiRISE images and the corresponding DEMs. Fig. 5 presents the images and samples we used. The North Craters sample set is closest to the landing site, being approximately 500–800 m to the north. The South Crater sample set is approximately 6 km away from the landing site and the South Crater 2 sample set is approximately 13 km south-southwest of the landing site. The Pitted Cone sample set is located approximately 25 km south-southeast of the landing site, among a cluster of possible pitted cones. Table 3 summarises the information of the HiRISE images and Table 4 lists the optical depths derived using the proposed method.

Fig. 6 presents the linear fit between modelled reflectance and that measured on the images. All dates have $R^2 > 0.94$, meaning the model describes the data well. The Pitted Cone set acquired on 7 October 2020, having a solar longitude (Ls) of 291.62°, was determined to have an optical depth of 0.670–0.779, depending on the photometric models. The South Crater 2 set acquired on 24 April 2021 (Ls of 36.02°), about 3 weeks before the landing, yielded an optical depth of 0.448–0.503, which implies a decrease from that of the Pitted Cone set. Almost a month after the landing, on 11 June 2021 (Ls of 57.51°), the optical depth estimated using the North Craters set ranged from 0.498 to 0.537, showing an increase. The South Crater set was collected from the HiRISE image acquired on 23 June 2021, when the Ls had increased to 62.44°. The resulting optical depth was 0.511–0.602, slightly higher than that obtained for the Ls of 57.51°. The average values and trend of the optical depth were plotted against days in Fig. 7. The results agree well with the results of previous studies for a large region around the Zhurong landing site before landing (Tang et al., 2021).

The retrieved optical depths were also compared with the dust column visible optical depth (DOD) at a wavelength of 670 nm predicted by the Mars Climate Database (MCD), which computes global meteorological parameters using the General Circulation Model (GCM) and observational data (Forget et al., 1999; Millour et al., 2018). The MCD predictions on the four sample dates (i.e., 7 October 2020, 24 April 2021 and 11 and 23 June 2021) were 0.869, 0.401, 0.362 and 0.351, respectively. These values are in general agreement with the results of

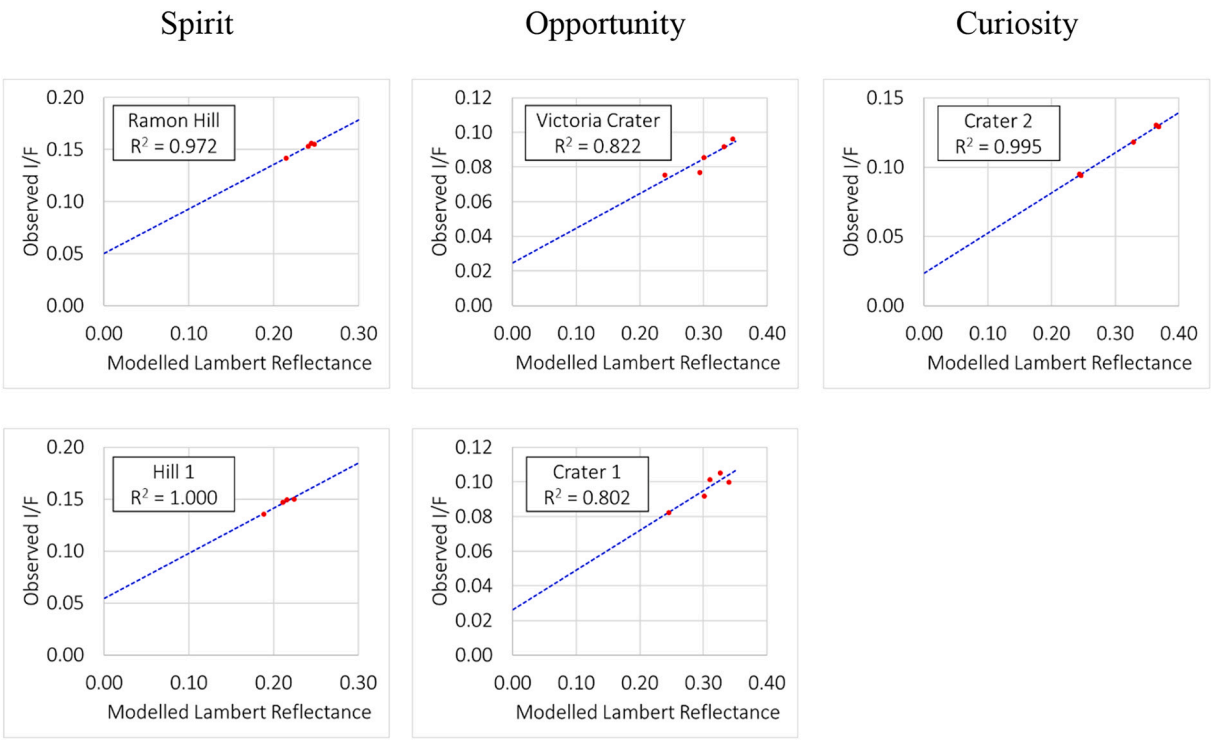

Fig. 4. Best fit lines of all sample sets at the retrieved τ based on the Lambert Model and scattering properties from Ockert-Bell et al. (1997). The data points are presented as red dots. (For interpretation of the references to colour in this figure legend, the reader is referred to the web version of this article.)

the proposed method, and the differences are within the reported deviations between MCD predictions and observations made by the MERs and CRISM (Montabone et al., 2015). We also tested the MCD predictions using the observations from the MERs and MSL as listed in Table 1, and found that the discrepancies can be up to >40%. Furthermore, the MCD is a global simulation model with a sparse spatial resolution (larger than 3°) whereas the proposed method is adopted for a specific time and location of the imagery, which may also contribute to the deviations. Nevertheless, in-situ observations acquired by the Zhurong rover would be helpful in further validating the findings and providing additional constraints for the GCM and the MCD.

We also tested the shadow method (Hoekzema et al., 2011; Tang et al., 2021) using this dataset. The shadows cast by the Tianwen-1 lander and the Zhurong rover were among the most distinctive shadows in the HiRISE imagery collected on 11 June 2021 (see Fig. 5) and they were used to derive optical depths. Using the shadow method and a correction factor (0.638 ± 0.071) (Tang et al., 2021), the resulting optical depth was found to lie between 0.666 and 0.832. We compared the values obtained by the shadow method and those reported by Tang et al. (2021) who also used the shadow method but with a different choice of shadows. Their results at a similar location and time showed an optical depth of approximately 0.4–0.6, in good agreement with our results (τ = 0.498–0.537). In contrast, τ = 0.666–0.832 obtained based on rover shadows are improbably large and do not agree with Tang et al. (2021)'s results. A possible reason for the large values is related to the correction factor, which was calibrated using shadows cast by relatively large landforms (Tang et al., 2021). However, such large shadows are not common at the Zhurong landing site. For further testing, we turned to the large crater located south-southeast of the landing site (see Fig. 5), which appears on the image acquired on 7 October 2020. The large crater has approximately 1 km in diameter and has a distinctive cast shadow within. Using the shadow method and the correction factor by Tang et al. (2021), we obtained τ_{Tang} = 0.756–0.946, in agreement with but slightly higher than the results from our approach (τ = 0.670–0.779). When considering the correction factor proposed by Hoekzema et al. (2011) (i.e., 0.71 ± 0.06), we obtained $\tau_{Hoekzema}$ = 0.697–0.825, consistent with our results. This analysis indicates that the correction factor for the shadow method might vary according to the types and characteristics of shadows used for calibration.

The above analysis of optical depths at the Zhurong landing site shows that the optical depths first decreased and then increased, with the turning point being around the landing date on 15 May 2021, indicating that the Zhurong rover landed at an appropriate time. This is in general consistent with seasonal variations of atmospheric dust activities on the northern hemisphere of Mars (Lemmon et al., 2015). If Zhurong had landed a few weeks later, the potentially more intense dust activity, as implied by the increased optical depth, may have posed an additional challenge to the landing mission. As the mission has continued, the Zhurong rover may have already observed in detail the dust activity of the southern Utopia Planitia. In this regard, repeated orbiter observations with Zhurong can provide further opportunities for joint space-ground analysis of Mars and its atmosphere.

4. Conclusions and discussion

This paper presented a method of retrieving the atmospheric optical depth from a single image for evaluating the pre and post-landing optical depths at the Zhurong landing site. The proposed method relies on a DEM co-registered to the image and an RTM that describes the photometric processes of the Martian atmosphere. Data for both the DEM and RTM are often readily available thanks to previous efforts of the scientific community. The proposed method uses only the illuminated regions of the Martian surface in the target image to calibrate aerosol path scattering parameters with the assistance of the DEM and then optimises the most probable optical depth using the RTM. The proposed method does not require additional observation data (e.g., CRISM data) acquired at a time similar to the acquisition time of the target image, nor does it require any effective shadows in the target image. The proposed method is therefore not limited by the availability of additional observations and does not require an abundance of shadows. We used a simplified TOA

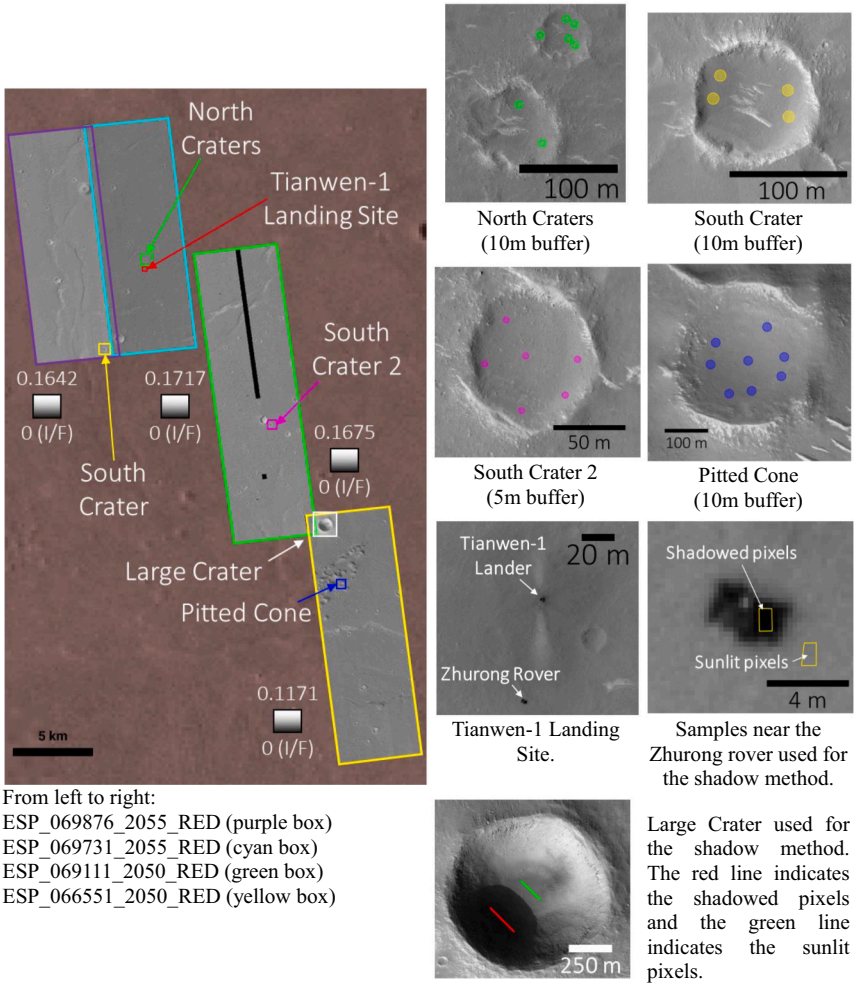

Fig. 5. Samples collected from the HiRISE images for analysing the Zhurong landing site. The images were overlaid on a Viking colour mosaic using JMARS (Christensen et al., 2009).

Table 3
Information of the HiRISE images used to analyse the Tianwen-1 landing site and the corresponding optical depth computed using the proposed method.

HiRISE Image ID	*ESP_066551_2050_RED*	*ESP_069111_2050_RED*	*ESP_069731_2055_RED*	*ESP_069876_2055_RED*
Acquisition Date	7 October 2020	24 April 2021	11 June 2021	23 June 2021
Local Time	14.71	15.24	15.60	15.56
Solar Longitude (Ls)	291.62°	36.02°	57.51°	62.44°
Incidence Angle	62.11°	46.64°	49.51°	48.69°
Emission Angle	4.88°	3.09°	5.51°	3.68°
Phase Angle	58.67°	49.72°	44.15°	52.24°

model for the DEM calibration procedure and the DISORT program as the RTM. We validated the proposed method using HiRISE red-band images and the co-registered HiRISE DEMs derived from photogrammetry. Measurements made from MERs and MSL observations at or near the time of image acquisition were used as a reference to assess the accuracy of the proposed method. We obtained sample sets from typical landforms such as craters and hills, the range of reflectance modelled from the DEM for each sample set is about 15–35%. We tested the approach using different sets of aerosol scattering Henyey-Greenstein phase function parameters and surface photometric models (i.e., the Lambert model, Lunar-Lambert model, and Minnaert model). The approach achieved RMSEs of <7% in most cases. The results showed that the optical depth retrievals are more sensitive to surface photometric models than to aerosol scattering parameters, which is reasonable because the data is optically thin and hence surface photometry has a greater influence on observed radiances. When analysing according to surface photometric models, the mean errors for all models were <7%. The Lambert and Minnaert models performed slightly better (having respective errors of <5% and <6% in most cases), possibly owing to the simplifications made to the TOA model and the representativeness of the photometric model used for the samples.

We applied the proposed method to the Zhurong landing site and presented the first optical depth estimate before and after the landing of Zhurong. The resulting optical depth was 0.670–0.779 on 7 October 2020, 0.448–0.503 on 24 April 2021, 0.498–0.537 on 11 June 2021, and 0.511–0.602 on 23 June 2021, having a first decreasing then increasing trend. The values and trends were in good agreement with the results of previous studies for similar regions and another retrieval method. The trend implies that there was a low optical depth when the lander landed on 15 May 2021 and that Zhurong may have since observed more

Table 4
Optical depth retrieved using the proposed method.

	Atmospheric Optical Depth			
	Lambert Model Ock/Tom/Chen	LL Model Ock/Tom/Chen	Minnaert Model Ock/Tom/Chen	Average ± σ
7 October 2020	0.683/	0.764/	0.749/	0.732 ±
ESP_066551_2050_RED	0.692/	0.779/	0.764/	0.038
	0.670	0.751	0.738	
24 April 2021	0.457/	0.493/	0.458/	0.470 ±
ESP_069111_2050_RED	0.461/	0.503/	0.467/	0.019
	0.448	0.490	0.455	
11 June 2021	0.517/	0.527/	0.500/	0.516 ±
ESP_069731_2055_RED	0.523/	0.537/	0.511/	0.012
	0.508	0.524	0.498	
23 June 2021	0.522/	0.592/	0.554/	0.556 ±
ESP_069876_2055_RED	0.526/	0.602/	0.564/	0.031
	0.511	0.586	0.549	

Note: "Ock" stands for the used scattering parameters reported by Ockert-Bell et al. (1997); "Tom" stands for those from Tomasko et al. (1999); and "Chen" stands for those from Chen-Chen et al. (2019).

intense dust activity in the southern Utopia Planitia. Furthermore, the resulting values can be compared with in-situ measurements of the rover as the latter becomes available.

The proposed approach is designed to be flexible to the configurations of the atmosphere. The current configuration considered the atmosphere as a single layer which is characterised by the Henyey-Greenstein phase function and a uniform diffuse skylight. Similar configurations were found in several other works (e.g., Vincendon et al., 2007; Petrova et al., 2012). Using a single-layered atmosphere is typically suitable for optically thin data ($\tau < 1$) (Petrova et al., 2012). This is in agreement with our results, in which the retrievals are more sensitive to surface photometry than to aerosol scattering parameters. There are more complex aerosol phase functions as alternatives to the Henyey-Greenstein function (e.g., the T-matrix model). Yet it is expected that using other choices has a limited impact on potential improvements because the data is optically thin and has low to moderate phase angles (Vincendon et al., 2013). On the other hand, sophisticated aerosol phase functions have explicit descriptions of the microphysical structure of the aerosols (e.g., effective grain size, shapes) (Wolff et al., 2009; Chen-Chen et al., 2019) and thus will be more suitable for in-depth analysis of the Martian atmosphere.

That said, the current simplified configurations can be suitable for optically thin data, quick assessments of local optical depths, and cartographic applications such as photometric normalization and 3D reconstruction. More sophisticated atmospheric configurations (e.g., multi-layered atmosphere, inhomogeneous pressure and temperature, T-matrix phase function) can be considered for optically thick data, or for such atmospheric sciences as constraining regional or global circulations and budget. On the other hand, retrievals can be sensitive to the atmospheric model at certain observation geometries due to the scattering surge produced by specific types and sizes of aerosols (Petrova et al., 2012). Ultimately, it is essential to understand the data and tinker with the model to improve robustness.

The constant albedo assumption is required by the linear model used for the fitting of image and DEM samples. Fitting algorithms that are robust to outliers (e.g., RANSAC) can be used to handle minor albedo variations of the samples. If a large group of samples with inhomogeneous albedo is used, ideally there still exists the most likely α_{DEM} which

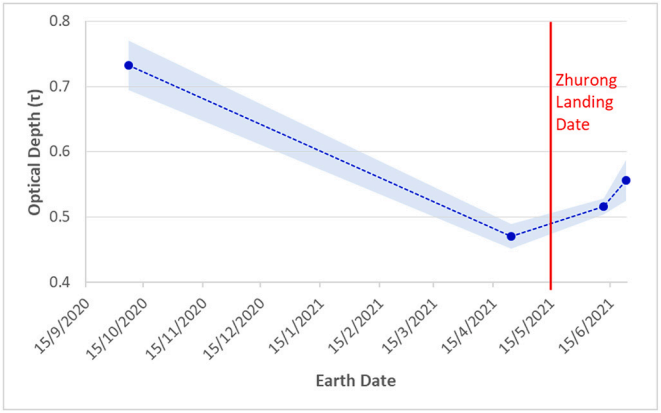

Fig. 7. Trend of the derived average optical depth around the Zhurong landing site plotted in Earth dates. The blue shaded ribbon indicates the error range of one standard deviation. The landing date of the Zhurong rover is indicated by the red line (15 May 2021). (For interpretation of the references to colour in this figure legend, the reader is referred to the web version of this article.)

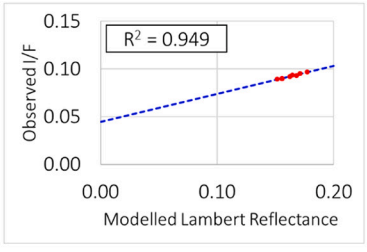

15 October 2020: *ESP_066551_2050_RED*

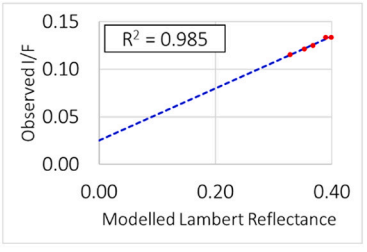

24 April 2021: *ESP_069111_2050_RED*

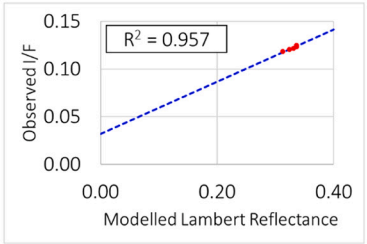

11 June 2021: *ESP_069731_2055_RED*

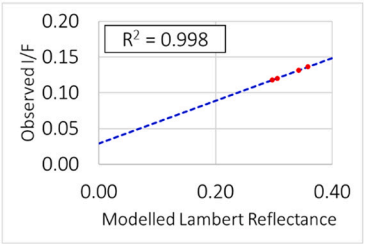

23 June 2021: *ESP_069876_2055_RED*

Fig. 6. Best fit lines of the samples used for the Zhurong landing site based on the Lambert Model. The data points are presented as red dots. (For interpretation of the references to colour in this figure legend, the reader is referred to the web version of this article.)

can be used by the proposed approach. In this case, however, a linear model can no longer be used and a new model for estimating α_{DEM} will be required.

The proposed method is highly complementary to applications such as the photoclinometric reconstruction of the Martian surface. To this end, it is worth testing the performance of the proposed method at multiple scales and resolutions. Understanding the criteria of best retrieval can facilitate automation, which would be helpful to increase the spatio-temporal resolution of the analysis of atmospheric dust variations with the proposed method.

Declaration of Competing Interest

The authors declare that they have no known competing financial interests or personal relationships that could have appeared to influence the work reported in this paper.

Acknowledgements

This work was supported by grants from the Research Grants Council of Hong Kong (RIF Project No: R5043-19, Project No: PolyU 15210520). The work was also supported by a grant from the China Academy of Space Technology (Project No: 17CPIT/HK0103). The authors would like to thank all those who worked on the archive of the datasets to make them publicly available.

References

Ceamanos, X., Douté, S., Fernando, J., et al., 2013. Surface reflectance of Mars observed by CRISM/MRO: 1. Multi-angle approach for retrieval of surface reflectance from CRISM observations (MARS-ReCO). J. Geophys. Res. Planets 118, 514–533.
Chen, Z., Wu, B., Liu, W.C., 2021. Mars3DNet: CNN-based high-resolution 3D reconstruction of the Martian surface from single images. Remote Sens. 13, 839.
Chen-Chen, H., Pérez-Hoyos, S., Sánchez-Lavega, A., 2019. Dust particle size and optical depth on Mars retrieved by the MSL navigation cameras. Icarus 319, 43–57.
Christensen, P.R., Engle, E., Anwar, S., et al., 2009. JMARS - a planetary GIS. In: American Geophysical Union, Fall Meeting 2009. Presented at the American Geophysical Union, Fall Meeting 2009, San Francisco, CA, USA. IN22A-06.
Colburn, D.S., Pollack, J.B., Haberle, R.M., 1989. Diurnal variations in optical depth at Mars. Icarus 79, 159–189.
D'Aversa, E., Oliva, F., Altieri, F., et al., 2021. Vertical distribution of dust in the Martian atmosphere: OMEGA/MEx limb observations. Icarus 371, 114702.
Davis, P.A., Soderblom, L.A., 1984. Modeling crater topography and albedo from monoscopic Viking orbiter images: 1. Methodol. J. Geophys. Res. 89, 9449.
Doute, S., Ceamanos, X., 2010. Retrieving Mars aerosol optical depth from CRISM/MRO imagery. In: 2010 2nd Workshop on Hyperspectral Image and Signal Processing: Evolution in Remote Sensing. Presented at the 2010 2nd Workshop on Hyperspectral Image and Signal Processing: Evolution in Remote Sensing (WHISPERS). IEEE, Reykjavik, Iceland, pp. 1–4.
Doute, S., Jiang, C., 2020. Small-scale topographical characterization of the Martian surface with in-orbit imagery. IEEE Trans. Geosci. Remote Sens. 58, 447–460.
Fairbairn, M.B., 2005. Planetary photometry: the Lommel-Seeliger law. J. R. Astron. Soc. Can. 99, 92–93.
Forget, F., Hourdin, F., Fournier, R., et al., 1999. Improved general circulation models of the Martian atmosphere from the surface to above 80 km. J. Geophys. Res. 104 (E10), 24155–24176.
Gebhardt, C., Abuelgasim, A., 2019. Scientific innovations from the Mars aerosol optical depth based on satellite data with a temporal resolution of hours. Prog Earth Planet Sci 6, 31.
Gehrke, S., 2008. Geometric and radiometric modeling of the martian surface based on object space matching and photoclinometry. In: The International Archives of the Photogrammetry, Remote Sensing and Spatial Information Sciences XXXVII-B4, pp. 1031–1036.
Hapke, B., 2012. Theory of Reflectance and Emittance Spectroscopy. Cambridge University Press, Cambridge, New York.
Hess, M., Wohlfarth, K., Grumpe, A., et al., 2019. Atmospherically compensated shape from shading on the Martian surface: towards the perfect digital terrain model of Mars. Int. Arch. Photogramm. Remote. Sens. Spat. Inf. Sci. XLII-2/W13, 1405–1411.
Hoekzema, N.M., Garcia-Comas, M., Stenzel, O.J., et al., 2010. Optical depth and its scale-height in Valles Marineris from HRSC stereo images. Earth Planet. Sci. Lett. 294, 534–540.
Hoekzema, N.M., Garcia-Comas, M., Stenzel, O.J., et al., 2011. Retrieving optical depth from shadows in orbiter images of Mars. Icarus 214, 447–461.
Johnson, J.R., Kirk, R., Soderblom, L.A., et al., 1999. Preliminary results on photometric properties of materials at the Sagan Memorial Station. Mars. J. Geophys. Res. 104, 8809–8830.
Kirk, R.L., Thompson, K.T., Becker, T.L., et al., 2000. Photometric modelling for planetary cartography. In: Presented at the 31st Lunar and Planetary Science Conference, Houston, Texas, U.S.A, p. 2025.
Kirk, R.L., Howington-Kraus, E., Rosiek, M.R., et al., 2008. Ultrahigh resolution topographic mapping of Mars with MRO HiRISE stereo images: meter-scale slopes of candidate Phoenix landing sites. J. Geophys. Res. 113, E00A24.
Lemmon, M.T., 2014. The Mars science laboratory optical depth record. In: Eighth International Conference on Mars, LPI Contributions, p. 1338.
Lemmon, M.T., Wolff, M.J., Smith, M.D., et al., 2004. Atmospheric imaging results from the Mars exploration rovers: Spirit and opportunity. Science 306, 1753–1756.
Lemmon, M.T., Wolff, M.J., Bell, J.F., et al., 2015. Dust aerosol, clouds, and the atmospheric optical depth record over 5 Mars years of the Mars exploration rover mission. Icarus 251, 96–111.
Li, Z., Wu, B., Liu, W.C., et al., 2021. Integrated photogrammetric and photoclinometric processing of multiple HRSC images for Pixelwise 3-D mapping on Mars. IEEE Trans. Geosci. Remote Sens. 1–13.
Liu, W.C., Wu, B., 2020. An integrated photogrammetric and photoclinometric approach for illumination-invariant pixel-resolution 3D mapping of the lunar surface. ISPRS J. Photogramm. Remote Sens. 159, 153–168.
Maki, J., Thiessen, D., Pourangi, A., et al., 2012. The Mars science laboratory engineering cameras. Space Sci. Rev. 170, 77–93.
McEwen, A.S., 1991. Photometric functions for photoclinometry and other applications. Icarus 92, 298–311.
McEwen, A.S., 1996. A precise lunar photometric function. Lunar Planet. Sci. 27, 841.
McEwen, A.S., Eliason, E.M., Bergstrom, J.W., et al., 2007. Mars reconnaissance Orbiter's high resolution imaging science experiment (HiRISE). J. Geophys. Res. 112, E05S02.
McGuire, P.C., Wolff, M.J., Smith, M.D., et al., 2008. MRO/CRISM retrieval of surface Lambert albedos for multispectral mapping of Mars with DISORT-based radiative transfer modeling: phase 1—using historical climatology for temperatures, aerosol optical depths, and atmospheric pressures. IEEE Trans. Geosci. Remote Sens. 46, 4020–4040.
Millour, E., Forget, F., Spiga, A., et al., 2018. THE MARS CLIMATE DATABASE (VERSION 5.3), Scientific Workshop: "From Mars Express to ExoMars", 27–28 Feb 2018. ESAC Madrid, Spain.
Minnaert, M., 1941. The reciprocity principle in lunar photometry. Astrophys. J. 93, 403.
Montabone, L., Forget, F., Millour, E., et al., 2015. Eight-year climatology of dust optical depth on Mars. Icarus 251, 65–95.
Neukum, G., Jaumann, R., Basilevsky, A., et al., 2009. HRSC: High resolution stereo camera. In: Mars Express: The Scientific Investigations. SP. ESA Communication Production Office, Noordwijk, The Netherlands, pp. 15–74.
Ockert-Bell, M.E., Bell, J.F., Pollack, J.B., et al., 1997. Absorption and scattering properties of the Martian dust in the solar wavelengths. J. Geophys. Res. 102, 9039–9050.
Petrova, E.V., Hoekzema, N.M., Markiewicz, W.J., et al., 2012. Optical depth of the Martian atmosphere and surface albedo from high-resolution orbiter images. Planet. Space Sci. 60, 287–296.
Pollack, J.B., Ockert-Bell, M.E., Shepard, M.K., 1995. Viking Lander image analysis of Martian atmospheric dust. J. Geophys. Res. 100, 5235.
Reiss, D., Hoekzema, N.M., Stenzel, O.J., 2014. Dust deflation by dust devils on Mars derived from optical depth measurements using the shadow method in HiRISE images. Planet. Space Sci. 93–94, 54–64.
Shkuratov, Y., Kaydash, V., Korokhin, V., et al., 2011. Optical measurements of the moon as a tool to study its surface. Planet. Space Sci. 59, 1326–1371.
Smith, M.D., 2004. Interannual variability in TES atmospheric observations of Mars during 1999–2003. Icarus 167, 148–165.
Smith, M.D., 2008. Spacecraft observations of the Martian atmosphere. Annu. Rev. Earth Planet. Sci. 36, 191–219.
Soderblom, J., Belliii, J., Hubbard, M., et al., 2006. Martian phase function: modeling the visible to near-infrared surface photometric function using HST-WFPC2 data. Icarus 184, 401–423.
Spiga, A., Forget, F., 2008. Fast and accurate estimation of solar irradiance on Martian slopes. Geophys. Res. Lett. 35, L15201.
Stamnes, K., Tsay, S.-C., Wiscombe, W., et al., 1988. Numerically stable algorithm for discrete-ordinate-method radiative transfer in multiple scattering and emitting layered media. Appl. Opt. 27, 2502.
Tang, Z., Liu, J., Wang, X., et al., 2021. The temporal variation of optical depth in the candidate landing area of China's Mars Mission (Tianwen-1). Remote Sens. 13, 1029.
Thomas, N., Markiewicz, W.J., Sablotny, R.M., et al., 1999. The color of the Martian sky and its influence on the illumination of the Martian surface. J. Geophys. Res. 104, 8795–8808.
Tomasko, M.G., Doose, L.R., Lemmon, M., et al., 1999. Properties of dust in the Martian atmosphere from the imager on Mars pathfinder. J. Geophys. Res. 104, 8987–9007.
Vincendon, M., 2013. Mars surface phase function constrained by orbital observations. Planet. Space Sci. 76, 87–95.
Vincendon, M., Langevin, Y., Poulet, F., et al., 2007. Recovery of surface reflectance spectra and evaluation of the optical depth of aerosols in the near-IR using a Monte Carlo approach: application to the OMEGA observations of high-latitude regions of Mars. J. Geophys. Res. 112.
Viúdez-Moreiras, D., Newman, C.E., Torre, M., et al., 2019. Effects of the MY34/2018 global dust storm as measured by MSL REMS in Gale crater. J. Geophys. Res. Planets 124, 1899–1912.
Wolff, M.J., Smith, M.D., Clancy, R.T., et al., 2009. Wavelength dependence of dust aerosol single scattering albedo as observed by the compact reconnaissance imaging spectrometer. J. Geophys. Res. 114, E00D04.
Wolff, M.J., Todd Clancy, R., Goguen, J.D., et al., 2010. Ultraviolet dust aerosol properties as observed by MARCI. Icarus 208, 143–155.

Wolkenberg, P., Giuranna, M., 2021. Daily dust variation from the PFS MEx observations. Icarus 353, 113823.
Wu, B., Liu, W.C., Grumpe, A., et al., 2018. Construction of pixel-level resolution DEMs from monocular images by shape and albedo from shading constrained with low-resolution DEM. ISPRS J. Photogramm. Remote Sens. 140, 3–19.
Wu, B., Dong, J., Wang, Y., et al., 2021. Characterization of the candidate landing region for Tianwen-1 – China's first Mission to Mars. Earth Space Sci. 8, 6.
Wu, B., Dong, J., Wang, Y., Rao, W., Sun, Z., Li, Z., et al., 2022. Landing site selection and characterization of Tianwen-1 (Zhurong rover) on Mars. J. Geophys. Res. Planets 127 (4) e2021JE007137.